Evolution of extremely large magnetoresistance in a Weyl semimetal, WTe_2 with Ni-doping

Abhishek Singh, Souvik Sasmal, Kartik K. Iyer, A. Thamizhavel, and Kalobaran Maiti*
Department of Condensed Matter Physics and Materials Science, Tata Institute of Fundamental Research, Homi Bhabha Road, Colaba, Mumbai-400005, India

(Received 14 June 2022; revised 11 November 2022; accepted 7 December 2022; published 23 December 2022)

WTe_2, a type-II Weyl semimetal, exhibits extremely large magnetoresistance (XMR) that is attributed to perfect electron-hole compensation. Here, we studied the evolution of the electronic properties of WTe_2 with Ni substitution at W sites. Transport measurements exhibit a metal-to-insulator transition at low temperatures with the application of magnetic field; the field-induced effect is significantly reduced in the doped sample. The XMR of about 10^6% at 2 K in WTe_2 is reduced to 10^4% in the 10% Ni-doped sample. The magnetoresistance shows an H^2 dependence and follows the temperature dependence of classical carrier mobility. We observe a deviation from Kohler's rule in both cases, indicating the presence of multiple types of charge carriers. Quantum oscillation data exhibit a signature of four Fermi pockets (two electron and two hole pockets) in both cases, and the nontrivial nature of the electron and hole bands. Interestingly, the electron-hole compensation is nearly perfect even in the doped compound, although the size of the Fermi pockets and the charge-carrier interaction parameters are slightly changed with doping. These results reveal intriguing insight into the XMR behavior of this class of materials and the possibilities of tuning the properties of charge carriers within the XMR regime.

DOI: 10.1103/PhysRevMaterials.6.124202

I. INTRODUCTION

Magnetoresistance (MR) is an interesting property of a material in that the electrical resistance changes with the application of a magnetic field. MR is defined by the percentage of the change in resistance, $\text{MR} = (R_H - R_0)/R_0 \times 100$ (R_H = resistance in the presence of a magnetic field, H, and R_0 is the resistance in the absence of the field). Materials with high MR have immense importance in advanced device technology involving sensors, switches, valves, memory storage devices in electronics and spintronics, etc. [1–4]. Usually, MR is small in simple metals, shows H^2 dependence at low fields, and saturates at high fields. Some materials show huge MR at low temperatures. For example, giant magnetoresistance (GMR) has been found in Fe/Cr superlattice [5,6], and colossal magnetoresistance (CMR) has been observed in manganese perovskites [7–9].

In addition to these magnetic materials, linear magnetoresistance (LMR) has been reported in some limited nonmagnetic materials where MR is independent of the magnetic property of the material [10–14]. Examples of such materials are topological insulators (i.e., Bi_2Se_3, Bi_2Te_3, SnTe), multilayer epitaxial graphene, Bi, silver chalcogenides (Ag_2Se/Te), and three-dimensional Dirac semimetals such as Cd_3As_2 [15–18]. Different mechanisms have been proposed to explain the origin of such MR in these exotic materials employing quantum/classical models [19,20]. In the quantum model, such a scenario can be achieved in the extreme quantum limits via application of a strong magnetic field that condenses all the carriers within the first Landau level [19]. On the other hand, in the classical model, LMR has been attributed to the inhomogeneity of the sample [20]. In Cd_3As_2, application of a strong magnetic field invalidates the topological protection from the backscattering mechanism, and hence large MR results [13].

Recently, WTe_2 was reported to exhibit extremely large magnetoresistance (XMR), as high as 1.3×10^7% with no signature of saturation up to 60 T at 0.53 K [1]. Perfect electron-hole (*e-h*) compensation is proposed to be an origin of XMR in WTe_2. Four electrons and four hole pockets along the Γ-X direction have been reported in a recent angle-resolved photoemission spectroscopy (ARPES) experiment [3]. Another report based on ARPES and quantum oscillation measurements suggested the presence of two electron pockets and two hole pockets of almost the same size, supporting the idea of carrier compensation for XMR [2]. ARPES study by Pletikosic *et al.* showed one electron and one hole pocket only [21]. Cai *et al.* have found two electron and two hole pockets in the quantum oscillations study, and they showed that application of pressure up to 23.6 kPa leads to an increase in size difference of the *e-h* pockets that reduces MR [22]. Xiang *et al.* reported the presence of one electron and two hole pockets from quantum oscillations studies [23]. Evidently, there is significant debate on the electronic structure and the underlying physics of the exoticity of this material, while all of these studies endorse the *e-h* compensation mechanism for XMR. Compensation between electron and hole concentrations should be sensitive to the doping of charge carriers. Keeping this in view, we studied the properties of Ni-doped WTe_2 and compared its properties with those of the parent compound. We discovered an interesting evolution of the properties of charge carriers with doping. Though MR reduces with doping, the value of MR is still very large in the doped compound.

*Corresponding author: kbmaiti@tifr.res.in

II. EXPERIMENTAL

Single crystals of $W_{1-x}Ni_xTe_2$ ($x = 0.0$, 0.1) were grown using the self-flux method. High-purity powder of W (99.999%), Te (99.999%), and Ni (99.999%) was mixed uniformly and placed in an alumina crucible, which was sealed in a quartz tube after evacuating down to $\sim 10^{-6}$ torr. The ratio of W to Te has been maintained as 1:12. The sealed tube was heated up to 1050 °C with a heating rate of 300 °C/h and then cooled down to 550 °C with a cooling rate of 2 °C/h, where the residual Te flux was decanted with a centrifuge. The resulting crystals were silver-colored and needlelike in morphology with the crystallographic c axis perpendicular to the crystal surface. The crystal structure of the samples was characterized by powder x-ray diffraction (XRD) after grinding part of the samples to fine powders. The XRD pattern shows a single phase for both cases, with no detectable impurity peak. The structure analysis suggests a $Pmn2_1$ space group with lattice constants $a = 6.457 \pm 0.019$ Å, $b = 3.459 \pm 0.005$ Å, and $c = 14.053 \pm 0.019$ Å for WTe_2. The lattice parameters estimated in the doped sample are $a = 6.452 \pm 0.010$ Å, $b = 3.458 \pm 0.004$ Å, and $c = 14.054 \pm 0.011$ Å; these values are very close to the pristine case. To find out the composition, we have carried out elemental analysis employing the energy-dispersive x-ray (EDX) technique. The compositions found from this analysis are $W_{1.003\pm0.046}Te_2$ and $W_{0.934\pm0.046}Ni_{0.076\pm0.005}Te_2$. Electrical resistivity and magnetoresistance as a function of magnetic field and temperature were measured using a standard four-probe technique in a Quantum Design Physical Property Measurement system (PPMS).

A. Results and discussion

Longitudinal resistivity (ρ_{xx}) as a function of temperature T at different external magnetic field H ($\parallel$ c-axis) is shown in Figs. 1(a) and 1(b) for the samples WTe_2 and $W_{0.9}Ni_{0.1}Te_2$, respectively. It is clear that ρ_{xx} show metallic behavior in both cases in the absence of a magnetic field. In WTe_2, the values of ρ_{xx} at 300 and 2 K are 2.25×10^{-6} and 3.19×10^{-9} Ω m, respectively, resulting in a residual resistance ratio (RRR) of 705, suggesting the excellent quality of the sample [1,22,24,25]. In $W_{0.9}Ni_{0.1}Te_2$, ρ_{xx} (300 K) and ρ_{xx} (2 K) are 2.66×10^{-6} and 2.67×10^{-8} Ω m with RRR = 100 due to chemical substitution induced disorder. The effect of disorder is manifested in the zero-field resistivity by an order of magnitude increment in the doped sample.

With the application of an external magnetic field, H (= 1 T), ρ_{xx} in WTe_2 shows a minima at a temperature T_m (~30 K) and then gradually increases akin to a semiconductor; resistivity appears to saturate at low temperatures [see the inset of Fig. 1(a)] [1,4,26,27]. The point of inflection in the rising part is defined as T_i. Such a magnetic-field-induced metal-to-insulator transition (MIT) makes this material a good candidate for application as low-temperature magnetic sensors and switches. $W_{0.9}Ni_{0.1}Te_2$ also exhibits MIT upon the application of a magnetic field, though the data at 1 T do not show MIT, as shown in the inset of Fig. 1(a). It appears that the scattering centers created due to Ni substitution reduce the magnetic-field-induced effect. The turn on behavior

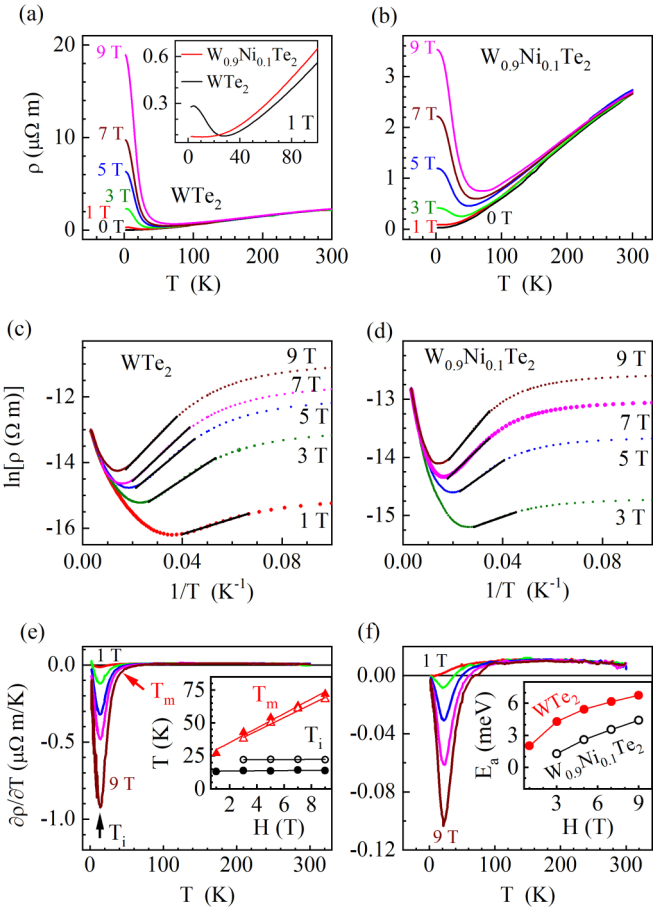

FIG. 1. Resistivity as a function of temperature at different applied magnetic field for (a) WTe_2 and (b) $W_{0.9}Ni_{0.1}Te_2$. The inset in (a) shows the resistivity at $H = 1$ T for the samples WTe_2 (black) and $W_{0.9}Ni_{0.1}Te_2$ (red). Plots of $\ln(\rho)$ vs T^{-1} at different magnetic fields for (c) WTe_2 and (d) $W_{0.9}Ni_{0.1}Te_2$. Black lines are the fit curve used to extract activation energy in the semiconducting region. $\partial\rho/\partial T$ vs T at different fields for the sample (e) WTe_2 and (f) $W_{0.9}Ni_{0.1}Te_2$. The inset in (e) shows the field dependence of T_i and T_m for WTe_2 (closed symbols) and $W_{0.9}Ni_{0.1}Te_2$ (open symbols). The inset in (f) show the activation energy estimated in (c) and (d): WTe_2 (closed circles) and $W_{0.9}Ni_{0.1}Te_2$ (open circles).

in $W_{0.9}Ni_{0.1}Te_2$ appears at a comparatively higher magnetic field, and the enhancement of resistivity is less pronounced in the doped case.

Following Arrhenius's law [27], the resistivity in the semiconducting regime can be expressed by $\rho = \rho_0 \exp(\frac{E_a}{K_B T})$, where ρ_0 is the resistivity at $T \to 0$ and E_a is the activation energy. To extract E_a, we plot $\ln(\rho)$ versus $(1/T)$ in Figs. 1(c) and 1(d) for WTe_2 and $W_{0.9}Ni_{0.1}Te_2$, respectively. Here, the black lines superimposed over the experimental data are the fit curves. The extracted activation energy E_a is shown in the inset of Fig. 1(f) exhibiting enhancement with the application of a magnetic field. Interestingly, the activation energy in the doped case is smaller than that in the pristine case. This suggests that the magnetic-field-induced localization effect is significantly lower in the doped sample.

In Figs. 1(e) and 1(f), we plot $\frac{\partial\rho}{\partial T}$ at different H for WTe_2 and $W_{0.9}Ni_{0.1}Te_2$, respectively. The inflection point, T_i, will

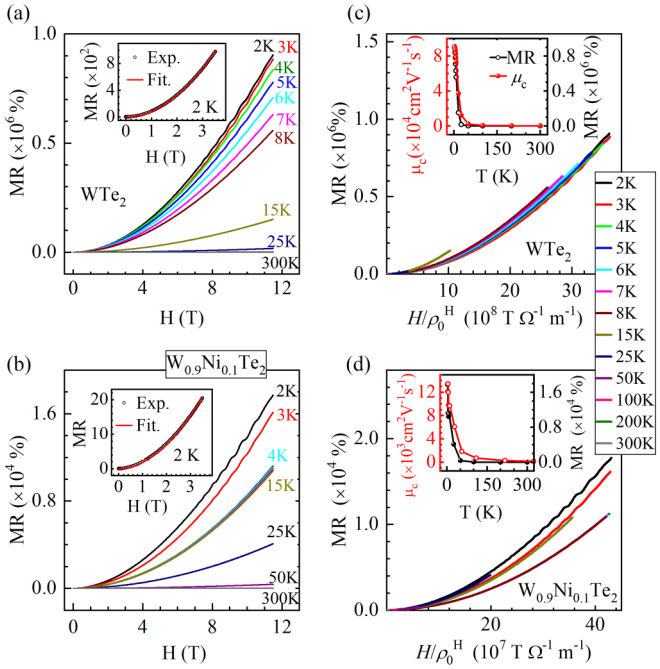

FIG. 2. Magnetoresistance (MR) as a function of applied magnetic field (H) at various temperatures for (a) WTe_2 and (b) $W_{0.9}Ni_{0.1}Te_2$. Insets in (a) and (b) are the MR fitting with the equation $MR = aH^k$ at 2 K. Kohler's plot at different temperatures for (c) WTe_2 and (d) $W_{0.9}Ni_{0.1}Te_2$ using the equation $MR = f(H/\rho_0^H)$. Insets in (c) and (d) are MR at 11.5 T field (solid circles) and mobility (open circles) as a function of temperature.

show a minimum in the $\frac{\partial\rho}{\partial T}$ plot, and T_m is the temperature where $\frac{\partial\rho}{\partial T}$ vanishes, as shown in the figure. The extracted T_i and T_m are shown in the inset of Fig. 1(e) as a function of magnetic field; closed symbols correspond to WTe_2 and open symbols represent $W_{0.9}Ni_{0.1}Te_2$. This provides a field-temperature phase diagram for the sample WTe_2 and $W_{0.9}Ni_{0.1}Te_2$. It is evident that with the increase of H, T_m increases rapidly but T_i remains almost unchanged in the entire field range studied. T_i for WTe_2 is found to be about 14 K, which becomes 23 K in $W_{0.9}Ni_{0.1}Te_2$. The slope of T_m is estimated to be 5.5 and 5.0 K/T for WTe_2 and $W_{0.9}Ni_{0.1}Te_2$, respectively. The area above the red lines ($T > T_m$) shows the metallic region where $\frac{\partial\rho}{\partial T} > 0$, and the MR value is very small. The region between the red and the black lines ($T_i < T < T_m$) represents a semiconducting nature with $\frac{\partial\rho}{\partial T} < 0$. In this region, MR is relatively high. The area below the black line ($T < T_i$) shows the plateau region where $\frac{\partial\rho}{\partial T} \to 0$, and MR reaches the extreme limit.

In Figs. 2(a) and 2(b), we study the magnetic field ($H \parallel c$) dependence of magnetoresistance at various temperatures for WTe_2 and $W_{0.9}Ni_{0.1}Te_2$, respectively. Maximum MR is found at the lowest temperature of 2 K and the highest applied field of 11.5 T, and no sign of saturation of MR is observed in both cases. The order of MR in WTe_2 reaches as high as 10^6%, which is consistent with the reported value [1,3,22–24]. Such a high MR demonstrates a strong response of the sample to the magnetic field as well as excellent quality of the crystal. In the case of $W_{0.9}Ni_{0.1}Te_2$, MR (= 10^4%) is reduced by two orders of magnitude. A similar type of work has been reported recently, in which aliovalent and isovalent substitutions are done at the tungsten site, and a reduced value of MR is observed [24]. In the absence of a magnetic field, ρ_{xx}(2 K) is higher in the Ni-doped sample as shown in Fig. 1. With the increase in magnetic field, resistivity increases more rapidly in the pristine case than in the doped case leading to an extremely high MR in WTe_2, while MR in the doped case is relatively lower. At 300 K, MR is found to be ∼2% for both samples, indicating a strong dependence on thermal scattering.

According to the semiclassical theory of transport, Kohler's rule predicts that MR follows a universal function of H/ρ_0^H in a metal containing a single type of charge carrier with temperature-independent carrier density; here ρ_0^H is the resistivity in the absence of field. Therefore, a plot of MR as a function of (H/ρ_0^H) at different temperatures should collapse onto a single curve [4,25,26]. The variation of MR as a function of (H/ρ_0^H) at various temperatures is shown in Figs. 2(c) and 2(d) for WTe_2 and $W_{0.9}Ni_{0.1}Te_2$, respectively. It is evident from the graphs that the MR deviates from Kohler's rule in both cases. Violation of Kohler's rule has been reported in some other XMR materials, too, such as WP_2, $TaAs_2$, TaAs, LaBi, $NbSb_2$, and $NbAs_2$ [26,28–31]. This indicates multiband contributions at the Fermi level and/or multiple scattering mechanisms [26].

In a compensated material, $MR = a_\circ(\mu_\circ H)^2$, here $\mu_\circ$ is the permeability of the sample and prefactor $a_\circ = \mu_h\mu_e$ is a constant; square root of a_0 provides the average classical mobility, μ_c. μ_h and μ_e are the hole and electron mobilities. This can easily be realized considering a two band model where resistivity ρ_{xx} can be expressed as $\rho_{xx} = \frac{1}{e}\frac{(n_h\mu_h+n_e\mu_e)+(n_h\mu_e+n_e\mu_h)\mu_h\mu_eB^2}{(n_h\mu_h+n_e\mu_e)^2+(n_h-n_e)\mu_h^2\mu_e^2B^2}$ [26]; the hole concentration n_h is equal to the electron concentration n_e. Therefore, we fit MR using the formula $MR = aH^k$ up to $H = 3.5$ T (beyond 3.5 T, quantum oscillations appear), here exponent k is a parameter. The fit results are shown in the insets of Figs. 2(a) and 2(b). The estimated value of k from the best fit is found to be 1.98 for WTe_2 and 1.95 for $W_{0.9}Ni_{0.1}Te_2$; such close to two exponent indicates charge carrier compensation in the samples. Thus, it appears that electron-hole compensation is close to perfect in both WTe_2 and $W_{0.9}Ni_{0.1}Te_2$ compounds.

The estimated average classical mobility [32] at various temperatures is shown together with the MR values at 11.5 T in the insets of Figs. 2(c) and 2(d). Our estimated values of mobility in the parent compound are consistent with the reported values [26,33]. The mobility in the $W_{0.9}Ni_{0.1}Te_2$ is significantly lower than that of the pristine sample presumably due to disorder-induced scattering. Mobility decreases with the increase in temperature in both cases due to the phonon contributions. Interestingly, the temperature evolution of the mobility is very similar to the temperature dependence of MR in both cases.

We now turn to the study of the doping effect on the Fermi surface employing the measurements of Shubnikov–de Hass (SdH) oscillations [34]. SdH oscillations are observed in the transport data due to the formation of Landau levels in the energy spectrum of the conduction electrons due to the application of a high magnetic field. In the present study, we observe such quantum oscillations at low

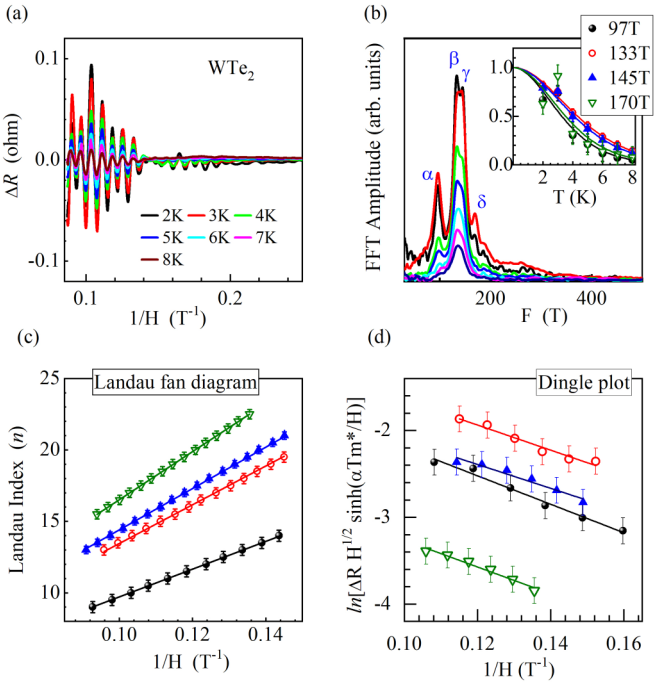

FIG. 3. (a) SdH oscillations and (b) corresponding FFT spectra of WTe_2 at different temperatures. The inset shows the normalized FFT amplitude as a function of temperature. The solid line is the fit using the LK formula. (c) Landau fan diagram. Lines represent the fit data for different frequencies. (d) Dingle plot of $\ln[\Delta R H^{1/2}\sinh(\alpha T m^*/H)]$ vs $1/H$; solid lines are the fit considering the Dingle formula.

temperatures and high magnetic fields in both samples. According to the Lifshitz-Kosevich (LK) formula, the amplitude of the oscillations can be expressed as [35] $\Delta R_{xx} \propto R_T R_D \cos[2\pi(n+\frac{1}{2}-\frac{\Phi_B}{2\pi}-\delta)]$. R_{xx} is the longitudinal resistance. The thermal damping factor R_T and the Dingle factor R_D are defined as $R_T = (\alpha T m^*/H)/[\sinh(\alpha T m^*/H)]$ and $R_D = \exp(-\alpha T_D m^*/H)$. Here, α $(= \frac{2\pi^2 k_B}{e\hbar})$ is a constant, m^* is the effective mass of the charge carriers, and T_D is the Dingle temperature. In the experiment, ΔR_{xx} is extracted by subtracting a smooth polynomial background from the R_{xx} data. ΔR_{xx} as a function of $1/H$ is shown in Fig. 3(a) for WTe_2 exhibiting a distinct signature of oscillations up to 8 K. The beating pattern of the oscillations indicates that more than one Fermi pocket is involved in the oscillations, which is also evident from Kohler's plot. Fast Fourier transform (FFT) of these oscillatory functions is shown in Fig. 3(b) exhibiting a signature of four distinct peaks at 97, 133, 145, and 170 T oscillation frequencies, labeled as α, β, γ, and δ. These oscillation frequencies are very similar to the earlier findings [22]. The sizes of the corresponding Fermi pockets are consistent with the ARPES results exhibiting signatures of two-hole pockets and two-electron pockets [33]. Comparing the sizes of the Fermi pockets in this study and ARPES results, we attribute α and δ to the hole pockets, and β and γ to the electron pockets. We have determined the extremal cross-section area of the Fermi surface, A_F, normal to the applied magnetic field using the Onsager relation, $F = \frac{\hbar}{2\pi e}A_F$; here F is the frequency of SdH oscillation. The estimated values of A_F for the Fermi pockets α, β, γ, and δ are 0.0093, 0.0127, 0.0139, and 0.0163 Å^{-2}, respectively [22,23]. The Fermi momentum k_F is estimated considering $A_F = \pi {k_F}^2$ and is found to be 0.0544, 0.0636, 0.0666, and 0.0720 Å^{-1}.

In an external magnetic field, the Landau quantization condition can be given by the Lifshitz-Onsager relation, $F/H = (n+\frac{1}{2}-\frac{\Phi_B}{2\pi}-\delta) = (n+\zeta)$, where n is the Landau level index, Φ_B is the Berry phase, and δ is a phase shift determined by the dimensionality of the system [35–39]. In conventional metals having parabolic dispersion, Φ_B is zero, and in Dirac or Weyl semimetals, $\Phi_B = \pi$. The parameter ζ can be determined from the Landau fan diagram, which lies between 0 and $(\pm 1/8)$ in a 3D Dirac semimetal or a Weyl semimetal having a nontrivial Berry phase [35–39]. A Landau fan diagram corresponding to different observed frequencies is shown in Fig. 3(c) for WTe_2 at 2 K. The symbols are the experimental data, and the superimposed solid lines show the fit results. The value of ζ is estimated from the intercept of the best linear fit of the Landau fan diagram, and it was found to be 0.010, −0.096, −0.054, and −0.031 for the α, β, γ, and δ pockets, respectively, suggesting a nontrivial Berry phase in WTe_2.

Following the LK formula, the effective mass of the charge carriers is determined by fitting the temperature dependence of the normalized FFT amplitudes. The inset in Fig. 3(b) shows the fit of the normalized oscillation amplitudes for WTe_2 considering an average H of 7.8 T; significant oscillations are observed in the magnetic field range of $4 \leqslant H \leqslant 11.5$ T in this study. The estimated value of the effective mass m^* for the α, β, γ, and δ pockets is found as $0.35m_e$, $0.27m_e$, $0.28m_e$, and $0.33m_e$ (m_e = bare electron mass) consistent with the reported values [23,40,41]. The Fermi velocity of the carriers is estimated using the relation $v_F = \frac{\hbar k_F}{m^*}$ [27] and is found to be 1.8×10^5, 2.7×10^5, 2.8×10^5, and 2.5×10^5 m/s [40–42].

The Dingle temperature T_D is determined from the slope of the linear fit of the Dingle plot, $\ln(\Delta R H^{1/2}\sinh(\alpha T m^*/H))$ versus $1/H$ shown in Fig. 3(d) [34,35,43]; here the symbols represent the experimental data at 2 K, and fits are shown by lines. Estimated T_D is found to be 3.18, 2.97, 3.46, and 3.78 K for the α, β, γ, and δ pockets, respectively [41]. The calculated value of the quantum scattering time, τ, using the relation $\tau = \frac{\hbar}{2\pi k_B T_D}$ [27] is 3.82×10^{-13}, 4.09×10^{-13}, 3.51×10^{-13}, and 3.22×10^{-13} s, respectively [42]. We have also calculated the mean free path for the carriers using the relation $l_q = v_F \tau$ [27], and we found it to be 69, 110, 98, and 81 nm for the pockets α, β, γ, and δ, respectively [42]. The estimated quantum mobility, μ_q, based on the relation $\mu_q = \frac{e\tau}{m^*}$ [27] is found to be 1918, 2663, 2204, and 1715 cm^2/V s, respectively [23,41]. The estimated quantum mobility is smaller than the classical mobility as often observed due to additional scattering processes not considered in the classical case [12,27,38]. The classical mobility is usually sensitive to large-angle scattering, while the quantum mobility is affected by all those processes that cause broadening in the Landau level [38]. The estimated carrier concentration using the formula n_{3D} $(= \frac{(2eF/\hbar)^{3/2}}{3\pi^2})$ has been found to be 5.44×10^{18}/cm^3, 8.73×10^{18}/cm^3, 9.93×10^{18}/cm^3, and 1.26×10^{19}/cm^3 for WTe_2. We have also calculated the ratio of electron to hole concentration, $\frac{n_e}{n_h} = \frac{n_{3D}(\beta)+n_{3D}(\gamma)}{n_{3D}(\alpha)+n_{3D}(\delta)}$, which is 1.03 in WTe_2, where n_e and n_h represent the total electron

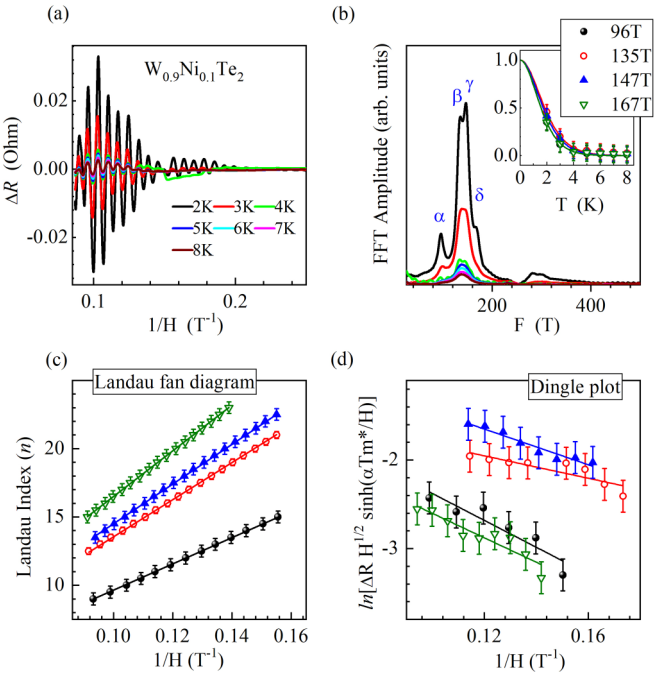

FIG. 4. (a) SdH oscillations in $W_{0.9}Ni_{0.1}Te_2$ at different temperatures. (b) Corresponding FFT spectra at different temperatures. The inset is the normalized FFT amplitude as a function of temperature. The solid line is the fit using LK formula. (c) Landau fan diagram. Lines represent the fit data for different frequencies. (d) Dingle plot of $\ln[\Delta R H^{1/2}\sinh(\alpha T m^*/H)]$ vs $1/H$; solid lines are the fit considering the Dingle formula.

and hole concentration. The total electron and hole densities are found to be $n_e \approx 1.866 \times 10^{19}/\text{cm}^3$ and $n_h \approx 1.805 \times 10^{19}/\text{cm}^3$. These estimations are verified by Hall resistivity measurements. The experimental Hall resistivity as a function of magnetic field at 5 K is simulated using the classical two-band model [26]. The extracted electron and hole carrier concentrations are found to be $1.36 \times 10^{19}/\text{cm}^3$ and $1.32 \times 10^{19}/\text{cm}^3$, respectively providing $n_e/n_h = 1.03$, which is similar to the estimation from SdH oscillations. These results suggest that electron-hole compensation is close to perfect in the pristine sample, which is consistent with the H^2 dependence of MR [inset Fig. 2(a)].

Now, we investigate the effect of Ni-doping on the SdH oscillation; variation of ΔR_{xx} as a function of $1/H$ is shown in Fig. 4(a). The corresponding FFT reveals four distinct frequencies at 96, 135, 147, and 167 T corresponding to α, β, γ, and δ Fermi pockets, respectively; these values are quite close to the estimated frequencies in WTe_2 [see Fig. 4(b)]. The Fermi surface area is found to be 0.0092, 0.0129, 0.0141, and 0.0160 Å^{-2}, respectively. The estimated Fermi momenta are 0.0541, 0.0641, 0.0670, and 0.0714 Å^{-1}, respectively.

A Landau fan diagram corresponding to different observed frequencies at 2 K is shown in Fig. 4(c). The estimated values of ζ for the α, β, γ, and δ pockets are 0.050, −0.020, −0.007, and −0.194, respectively. Clearly, the Berry phase for α, β, and γ pockets is close to π, indicating that the nontrivial nature of the hole and electron bands survives in the doped compound. A slight deviation is observed in the case of δ-band. The estimated effective mass for α, β, γ, and

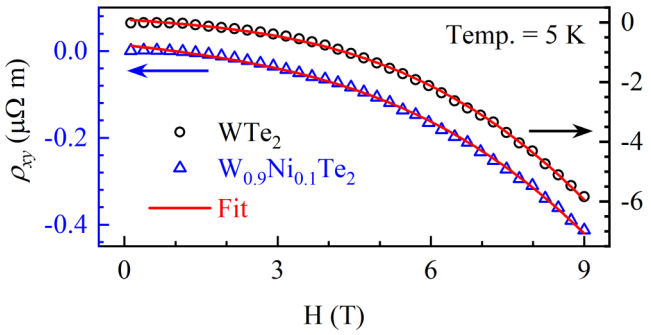

FIG. 5. ρ_{xy} as a function of H in WTe_2 (open circles) and $W_{0.9}Ni_{0.1}Te_2$ (open triangles). The solid lines superimposed over the experimental data represent the corresponding fitting by the two-band model.

δ is $0.74m_e$, $0.63m_e$, $0.67m_e$, and $0.74m_e$, respectively, which is somewhat larger than those in WTe_2; the corresponding fits are shown in the inset of Fig. 4(b). The calculated Fermi velocities (8.5×10^4, 1.2×10^5, 1.2×10^5, and 1.1×10^5 m/s) are reduced slightly in the doped sample.

While all the above results are in line with the expected behavior due to chemical substitutional disorder, the estimated Dingle temperatures are found to be smaller in the doped sample ($T_D = 1.39$, 0.70, 1.02, and 1.26 K for the α, β, γ, and δ pockets). This leads to an estimation of enhanced scattering time, τ (8.75×10^{-13}, 1.74×10^{-12}, 1.19×10^{-12}, and 9.65×10^{-13} s), l_q (74, 204, 138, and 108 nm), and mobility (2074, 4847, 3128, and 2293 $\text{cm}^2/\text{V s}$). Understanding the underlying physics of such anomalous behavior requires further studies in this direction. We estimated the carrier concentration in both cases to investigate the effect of doping. The carrier concentration in the Ni-doped sample is $5.35 \times 10^{18}/\text{cm}^3$, $8.93 \times 10^{18}/\text{cm}^3$, $1.01 \times 10^{19}/\text{cm}^3$, and $1.23 \times 10^{19}/\text{cm}^3$, respectively. The total electron and hole densities in this sample are $n_e \approx 1.903 \times 10^{19}/\text{cm}^3$ and $n_h \approx 1.763 \times 10^{19}/\text{cm}^3$. This suggests that hole concentration is slightly decreased and electron concentration is increased due to Ni-substitution. The ratio of total electron to hole concentration is 1.08 in the Ni-doped case, which is close to 1, indicating that the *e-h* compensation condition is closely maintained even in the Ni-doped compound, which could be the reason for such a high MR.

We have verified the above estimations using Hall measurements. Experimental Hall resistivity ρ_{xy} as a function of magnetic field, H, collected at a temperature of 5 K is shown in Fig. 5. The data for WTe_2 are represented by open circles, and those for $W_{0.9}Ni_{0.1}Te_2$ are shown by open triangles. Red lines superimposed over the experimental data show the fitting by the classical two-band model [26]. The electron and hole concentrations are found to be $1.34 \times 10^{19}/\text{cm}^3$ and $1.33 \times 10^{19}/\text{cm}^3$, respectively, resulting in $n_e/n_h = 1.01$. These numbers are consistent with the carrier concentrations estimated from the SdH oscillations.

III. CONCLUSIONS

In summary, we have grown high-quality single crystals of $W_{0.9}Ni_{0.1}Te_2$ ($x = 0.0$, 0.1) using the self-flux method. Under

the application of an external magnetic field, a metal-insulator transition has been found in temperature-dependent resistivity in both compounds. Magnetotransport study exhibits nonsaturating parabolic XMR and evidence of electron-hole compensation. The XMR ($= 10^6\%$) in WTe_2 at 11.5 T field and 2 K temperature is reduced to about $10^4\%$ with Ni-doping; the MR follows the temperature dependence of classical mobility in both cases. The nontrivial topological nature of the charge carriers has been confirmed from the estimated Berry phase in the Landau fan diagram for the Fermi pockets present in both samples. Ni-substitution influences various interaction parameters, such as effective mass, mobility, scattering time, etc. The electron-hole compensation is found to be closely maintained even in the doped sample. While mobility appears to be one of the key parameters deriving the XMR property in this system, further studies are required to understand the underlying physics. These results reveal a unique property of this class of materials where one can tune the properties of charge carriers maintaining the XMR property of the material required for advanced technology.

ACKNOWLEDGMENTS

A.S. acknowledges financial support from SERB, Government of India, under the Project No. PDF/2018/003558. Financial support from DAE, Govt. of India (Project Identification No. RTI4003, DAE OM No. 1303/2/2019/R&D-II/DAE/2079 dated 11-02-2020) is thankfully acknowledged. K.M. acknowledges financial assistance from DAE under the DAE-SRC-OI Award program.

[1] M. N. Ali, J. Xiong, S. Flynn, J. Tao, Q. D. Gibson, L. M. Schoop, T. Liang, N. Haldolaarachchige, M. Hirschberger, N. P. Ong, and R. J. Cava, Nature (London) **514**, 205 (2014).

[2] Y. Wu, N. H. Jo, M. Ochi, L. Huang, D. Mou, S. L. Budko, P. C. Canfield, N. Trivedi, R. Arita, and A. Kaminski, Phys. Rev. Lett. **115**, 166602 (2015).

[3] J. Jiang, F. Tang, X. C. Pan, H. M. Liu, X. H. Niu, Y. X. Wang, D. F. Xu, H. F. Yang, B. P. Xie, F. Q. Song, P. Dudin, T. K. Kim, M. Hoesch, P. K. Das, I. Vobornik, X. G. Wan, and D. L. Feng, Phys. Rev. Lett. **115**, 166601 (2015).

[4] Y. L. Wang, L. R. Thoutam, Z. L. Xiao, J. Hu, S. Das, Z. Q. Mao, J. Wei, R. Divan, A. Luican-Mayer, G. W. Crabtree, and W. K. Kwok, Phys. Rev. B **92**, 180402(R) (2015).

[5] G. Binasch, P. Grünberg, F. Saurenbach, and W. Zinn, Phys. Rev. B **39**, 4828 (1989).

[6] M. N. Baibich, J. M. Broto, A. Fert, F. Nguyen Van Dau, F. Petroff, P. Etienne, G. Creuzet, A. Friederich, and J. Chazelas, Phys. Rev. Lett. **61**, 2472 (1988).

[7] A. P. Ramirez, R. J. Cava, and J. Krajewski, Nature (London) **386**, 156 (1997).

[8] Y. Moritomo, A. Asamitsu, H. Kuwahara, and Y. Tokura, Nature (London) **380**, 141 (1996).

[9] A. Urushibara, Y. Moritomo, T. Arima, A. Asamitsu, G. Kido, and Y. Tokura, Phys. Rev. B **51**, 14103 (1995).

[10] A. L. Friedman, J. L. Tedesco, P. M. Campbell, J. C. Culbertson, E. Aifer, F. K. Perkins, R. L. Myers-Ward, J. K. Hite, C. R. Eddy Jr., G. G. Jernigan, and D. K. Gaskill, Nano Lett. **10**, 3962 (2010).

[11] Y. Zhao, H. Liu, C. Zhang, H. Wang, J. Wang, Z. Lin, Y. Xing, H. Lu, J. Liu, Y. Wang, S. Jia, X. C. Xie, and J. Wang, Phys. Rev. X **5**, 031037 (2015).

[12] A. Narayanan, M. D. Watson, S. F. Blake, N. Bruyant, L. Drigo, Y. L. Chen, D. Prabhakaran, B. Yan, C. Felser, T. Kong, P. C. Canfield, and A. I. Coldea, Phys. Rev. Lett. **114**, 117201 (2015).

[13] T. Liang, Q. Gibson, M. N. Ali, M. Liu, R. J. Cava, and N. P. Ong, Nat. Mater. **14**, 280 (2015).

[14] R. Xu, A. Husmann, T. F. Rosenbaum, M. L. Saboungi, J. E. Enderby, and P. B. Littlewood, Nature (London) **390**, 57 (1997).

[15] Y. Zhao, C. Z. Chang, Y. Jiang, A. DaSilva, Y. Sun, H. Wang, Y. Xing, Y. Wang, K. He, X. Ma, Q.-K. Xue, and J. Wang, Sci. Rep. **3**, 3060 (2013).

[16] X. Wang, Y. Du, S. Dou, and C. Zhang, Phys. Rev. Lett. **108**, 266806 (2012).

[17] H. Tang, D. Liang, R. L. Qiu, and X. P. Gao, ACS Nano **5**, 7510 (2011).

[18] S. Baral and A. Lakhani, AIP Conf. Proc. 2220 [3rd International Conference on Condensed Matter and Applied Physics (ICC-2019); edited by M. N. Shekhawat, S. Bharadwaj, and B. Suthar] (AIP, New York, 2020), p. 060006; A. Maiti, R. P. Pandeya, B. Singh, K. K. Iyer, A. Thamizhavel, and K. Maiti, Phys. Rev. B **104**, 195403 (2021); A. Maiti, A. Singh, K. K. Iyer, and A. Thamizhavel, Appl. Phys. Lett. **120**, 112102 (2022); S. Baral, M. K. Dasoundhi, I. Rajput, D. Kumar, and A. Lakhani, Phys. Status Solidi (RRL) **16**, 2100542 (2022).

[19] A. A. Abrikosov, Phys. Rev. B **58**, 2788 (1998).

[20] M. M. Parish and P. B. Littlewood, Nature (London) **426**, 162 (2003).

[21] I. Pletikosic, M. N. Ali, A. V. Fedorov, R. J. Cava, and T. Valla, Phys. Rev. Lett. **113**, 216601 (2014).

[22] P. L. Cai, J. Hu, L. P. He, J. Pan, X. C. Hong, Z. Zhang, J. Zhang, J. Wei, Z. Q. Mao, and S. Y. Li, Phys. Rev. Lett. **115**, 057202 (2015).

[23] F. X. Xiang, M. Veldhorst, S. X. Dou1 and X. L. Wang, Europhys. Lett. **112**, 37009 (2015).

[24] Y. Y. Lv, B. B. Zhang, X. Li, B. Pang, F. Zhang, D. J. Lin, J. Zhou, S. H. Yao, Y. B. Chen, S. T. Zhang, M. Lu, Z. Liu, Y. Chen, and Y. F. Chen, Sci. Rep. **6**, 26903 (2016); S. Flynn, M. Ali, and R. J. Cava, arXiv:1506.07069.

[25] Y. Zhao, H. Liu, J. Yan, W. An, J. Liu, X. Zhang, H. Wang, Y. Liu, H. Jiang, Q. Li, Y. Wang, X.-Z. Li, D. Mandrus, X. C. Xie, M. Pan, and J. Wang, Phys. Rev. B **92**, 041104(R) (2015).

[26] Y. Y. Lv, X. Li, J. Zhang, B. Pang, S. S. Chen, L. Cao, B.-B. Zhang, D. Lin, Y. B. Chen, S. H. Yao, J. Zhou, S. T. Zhang, M. H. Lu, M. Tian, and Y. F. Chen, Phys. Rev. B **97**, 245151 (2018).

[27] F. F. Tafti, Q. Gibson, S. Kushwaha, J. W. Krizan, N. Haldolaarachchige, and R. J. Cava, Proc. Natl. Acad. Sci. (USA) **113**, E3475 (2016).

[28] S. Sun, Q. Wang, P. J. Guo, K. Liu, and H. Lei, New J. Phys. **18**, 082002 (2016).

[29] Z. Yuan, H. Lu, Y. Liu, J. Wang, and S. Jia, Phys. Rev. B **93**, 184405 (2016).

[30] C. L. Zhang, Z. Yuan, Q. D. Jiang, B. Tong, C. Zhang, X. C. Xie, and S. Jia, Phys. Rev. B **95**, 085202 (2017).
[31] K. Wang, D. Graf, L. Li, L. Wang, and C. Petrovic, Sci. Rep. **4**, 7328 (2014).
[32] D. Das, K. Malik, S. Bandyopadhyay, D. Das, S. Chatterjee, and A. Banerjee, Appl. Phys. Lett. **105**, 082105 (2014).
[33] Z. Zhu, X. Lin, J. Liu, B. Fauqué, Q. Tao, C. Yang, Y. Shi, and K. Behnia, Phys. Rev. Lett. **114**, 176601 (2015).
[34] D. Shoenberg, *Magnetic Oscillations in Metals* (Cambridge University Press, Cambridge, UK, 2009).
[35] Y. Liu, X. Yuan, C. Zhang, Z. Jin, A. Narayan, C. Luo, Z. Chen, L. Yang, J. Zou, X. Wu, S. Sanvito, Z. Xia, L. Li, Z. Wang, and F. Xiu, Nat. Commun. **7**, 12516 (2016).
[36] F. X. Xiang, X. L. Wang, M. Veldhorst, S. X. Dou, and M. S. Fuhrer, Phys. Rev. B **92**, 035123 (2015).
[37] L. Zhou, A. Ramiere, P. B. Chen, J. Y. Tang, Y. H. Wu, X. Lei, G. P. Guo, J. Q. He, and H. T. He, New J. Phys. **21**, 093009 (2019).
[38] R. Singha, A. K. Pariari, B. Satpati, and P. Mandal, Proc. Natl. Acad. Sci. (USA) **114**, 2468 (2017).
[39] A. P. Sakhya, P. L. Paulose, A. Thamizhavel, and K. Maiti, Phys. Rev. Mater. **5**, 054201 (2021); A. P. Sakhya, S. Kumar, A. Pramanik, R. P. Pandeya, R. Verma, B. Singh, S. Datta, S. Sasmal, R. Mondal, E. F. Schwier, K. Shimada, A. Thamizhavel, and K. Maiti, Phys. Rev. B **106**, 085132 (2022).
[40] R. Bi, Z. Feng, X. Li, J. Zhao, J. Fan, Y. Shi, D. Yu, and X. Wu, Phys. Rev. B **100**, 235405 (2019).
[41] J. Meng, X. Chen, M. Liu, W. Jiang, Z. Zhang, J. Ling, T. Shao, C. Yao, L. He, R. Dou, C. Xiong, and J. Nie, J. Phys.: Condens. Matter **32**, 355703 (2020).
[42] P. Li, Y. Wen, X. He, Q. Zhang, C. Xia, Z. M. Yu, S. A. Yang, Z. Zhu, H. N. Alshareef, and X. X. Zhang, Nat. Commun. **8**, 2150 (2017).
[43] G. Xu, A. D. Visser, Y. Huang, and X. Mao, Adv. Condens. Matter Phys. **2019**, 5628685 (2019).